Proceedings of the ASME 2024
Aerospace Structures, Structural Dynamics, and Materials Conference
SSDM2024
April 29 - May 1, 2024, Renton, Washington

SSDM2024-121566

ADAPTIVE-STIFFNESS CHARACTERISTICS OF PNEUMATIC ROTARY ACTUATORS FOR FOLDING WINGTIPS

Patrick Meyer[†,*], **Moritz Sprengholz**[†], **Hendrik Traub**[†], **Christian Hühne**

Technische Universität Braunschweig, Institute of Mechanics and Adaptronics, Braunschweig, Germany

ABSTRACT

Folding wingtips address the challenges of high aspect ratio wings, such as airport conformity, increased wing root bending moment, and reduced aircraft maneuverability. The functionalities of free-flapping folding wingtips can be extended with multifunctional wingtip actuators that allow for active adjustment of the wingtip's cant angle and hinge stiffness. The objective of this paper is the identification of governing factors influencing the adaptive-stiffness characteristics of pneumatic rotary actuators. The authors experimentally determine the characteristics of such a commercially available pneumatic rotary actuator and formulate analytical equations for actuator moment and stiffness as well as the wingtip's natural frequencies. The actuator characteristics can be accurately described by an isobaric or adiabatic process, depending on the pneumatic setup. The pneumatic actuator exhibits zero stiffness in a pressure-regulated mode, whereas targeted adjustment of the actuator stiffness is possible by shutting off the mass flow into the actuator chambers. The formulated equations allow a detailed design of multifunctional wingtip actuators for application in highly efficient high aspect ratio aircraft. The findings of this study can be transferred to hydraulic rotary actuators, which would be required to achieve the necessary load-bearing capacity for application in larger transport aircraft.

Keywords: folding wingtip, aeroelastic hinge, load alleviation, pneumatic actuation, adaptive stiffness, wingtip device, morphing wing

1. INTRODUCTION

High aspect ratio wings improve the aircraft's efficiency by reducing its induced drag, reducing fuel burn and noise emissions [1]. However, increased span is accompanied by disadvantages, such as increased wing root bending moment (WRBM), reduced aircraft maneuverability, and violations of airport conformity. Airport conformity refers to wingspan restrictions imposed by airport operating rules and is regulated by the *aerodrome reference code* [2] of the International Civil Aviation Organization (ICAO) or the *airplane design group* [3] of the Federal Aviation Administration (FAA). Increased WRBM necessitates reinforcing the wing structure adding additional mass, whereas reduced maneuverability places demands on the design of the flight control surfaces. This is further complicated because the installation space for control surfaces at the tips of slender flexible wings is severely limited and ailerons are less effective due to higher wing deformations.

A recent trend to face the challenges of high aspect ratio (HAR) wings is using folding wingtip devices, as schematically shown in Fig. 1. Nevertheless, folding the wings to comply with on-ground size restrictions is by no means completely new. Carrier-based aircraft have been equipped with folding wings for decades to meet extreme storage requirements, such as the Grumman F4F-4 Wildcat developed in 1941 [4]. With the Boeing 777X, folding wings have recently found their way into commercial aviation. The Boeing 777X, first flown in 2020, is equipped with folding wingtips (FWTs) that can fold upward on ground to comply with the airport's space limitations. With its wingtips folded upward, the aircraft meets the 65 m wingspan limit of ICAO's aerodrome reference code letter E, allowing the same gates to be used as with the original Boeing 777, whereas unfolding the wingtips increases the wingspan by 7 m, i.e. 10%, in flight [5].

Beyond folding the wingtips on ground to comply with airport size restrictions, in-flight FWTs allow for adapting the wing's lift coefficient to changing flight conditions, improving aircraft performance and efficiency. Passive in-flight FWTs enable passive load alleviation and roll damping alleviation, whereas active in-flight FWTs allow mission adaptability, active load alleviation, and advanced flight control [6]. A recent example of passive in-flight FWTs is Airbus' AlbatrossONE flight demonstrator [7]. With the AlbatrossONE, Airbus is investigating free-flapping wingtip devices with aeroelastic hinges that can be unlocked in flight to enable passive load alleviation. The capabilities of free-flapping wingtips have been demonstrated in flight tests in 2019 [7] and 2020 [8] with the AlbatrossOne proving the concept of the semi-aeroelastic hinge (SAH). An outwards-pointing hinge

[†]Joint first authors
[*]Corresponding author: pat.meyer@tu-braunschweig.de

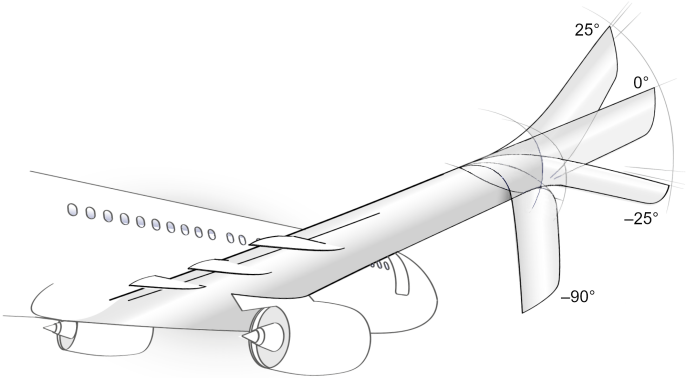

FIGURE 1: SCHEMATIC REPRESENTATION OF AN AIRCRAFT WITH FOLDING WINGTIPS.

line improves the load alleviation capability because upward folding of the wingtips then induces a reduction of the local angle of incidence [9]. The SAH is currently being further examined on a larger scale with Airbus' *eXtra Performance Wing* demonstrator that is based on a Cessna Citation VII business jet [10].

Two examples of aircraft equipped with active in-flight FWTs are the XB-70 Valkyrie [11] or NASA's prototype-technology evaluation and research aircraft (PTERA) [12]. These aircraft slowly adapt their wing shape in flight by wingtip folding to improve the aircraft's aerodynamics during changing flight conditions. Unlike slowly actuated wingtips, fast actuated wingtips with asymmetric deflection enable advanced flight control by generating roll moment. So far, however, actuated wingtips used as control surfaces have only been investigated for unmanned aerial vehicles (UAVs) and small-scale aircraft, such as in the experimental study of Mills et al. [13]. A comprehensive review on in-flight folding and morphing wingtips is presented in [6].

Further improvement in aircraft efficiency and flight performance would be possible with a multifunctional wingtip actuator that combines the functionalities of passive and active FWTs in one single system. A stiffness-adaptive wingtip with an aeroelastic hinge that is actively adjustable in flight allows for active adjustment of the wingtip's cant angle and hinge stiffness. Such a combined system is referred to by the authors as *actuated adaptive wingtips* [6] and clears the path for the incorporation of additional functionalities such as advanced flight control, mission adaptability, enhanced load alleviation, and flutter suppression. Moreover, the possibility of setting actuator moment and actuator stiffness independently of each other eliminates the need for a wingtip locking mechanism, while the defined stiffness permanently enables effective gust load alleviation without requiring gust detection. Such a system is also not faced with the challenge of timing the hinge release for effective alleviation of peak loads, as is the case with free-flapping wingtips [14].

Whereas previous research of the authors investigated a morphing wingtip device based on pressure-actuated cellular structures (PACS) to enable adaptive stiffness and active deflection [6, 15], this paper presents a more simplified actuator design. Although PACS are distinguished by outstanding load-bearing capacity and significant stiffness adaptivity, such cellular structures require considerable effort in their design and fabrication, as they consist of multiple rows of pressurized polygonal cells with rigid walls connected by thin-walled flexure hinges [16]. The simplified design of the actuated adaptive wingtip hinge examined in this study is based on a pneumatic rotary actuator with two antagonistic pistons connected by gear racks and a pinion. Pneumatic rotary actuators are commercially available in various sizes and with various actuator moments.

In this paper, the authors provide fundamental interrelationships of antagonistic pneumatic actuators in terms of basic analytical equations and experimentally determined actuator characteristics. The authors identify the quasi-static operating envelope and preliminary dynamic characteristics of the pneumatic actuator by applying a set of input pressures and actuator moments on a custom-made pneumatic test stand. The main goal of this study is the identification of governing factors influencing the moment, stiffness, and natural frequencies of pneumatic rotary actuators. The adaptive-stiffness characteristics of the wingtip hinge can be obtained from the actuator's working graph and allow interpretation for scaling the actuator for application in wingtip structures. A potential option for future developments involves switching from a pneumatic to a hydraulic rotary actuator, where the same principles can be applied but at increased absolute stiffnesses and moments.

This paper is structured as follows: Section 2 describes the pneumatic rotary actuator, the test stand, and the test matrix. The test results with a focus on actuator stiffness, moment, and natural frequencies are presented in Section 3. Section 4 draws implications for implementing pneumatic rotary actuators as multifunctional wingtip actuators, whereas Section 5 summarizes this paper and highlights future research.

2. METHODS

For pneumatic actuators with two antagonistic pistons, the actuator moment can be decoupled from its stiffness. Actuator moment is only a function of the pressure difference between both actuator chambers, whereas stiffness, and thus deflection, depends on the total pressure level and volume in both chambers. This enables operation in an adaptive-stiffness mode under specific conditions. Consequently, pneumatic actuation offers great potential for realizing shape-morphing structures featuring significant stiffness adaptivity and shape-changing capacity. The following subsections will detail the selected pneumatic rotary actuator, the design of the test stand, and the test matrix used to characterize the quasi-static and dynamic properties of the pneumatic actuator.

2.1 Pneumatic Rotary Actuator

This study uses a commercially available pneumatic rotary actuator. The focus of this study is to reveal fundamental interrelationships of pneumatic adaptive-stiffness actuators rather than to design a wingtip actuator with consideration of realistic flight loads. Therefore, the selected actuator is not intended to represent a scaled version of an aeroelastic hinge for folding wingtips, and the absolute values of achievable actuator moments and stiffnesses as well as actuator mass and size are not important at this design stage. However, possible options for scaling the pneumatic actuator to real aircraft loads are provided in Section 4.

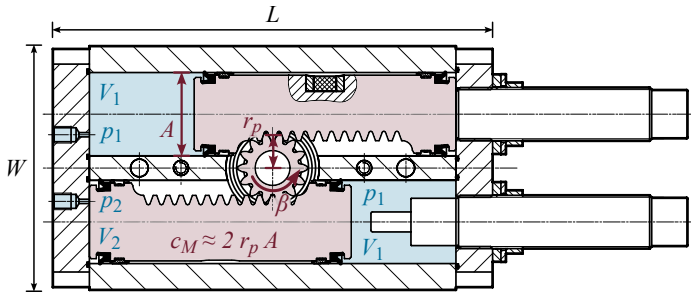

FIGURE 2: CROSS-SECTIONAL VIEW OF THE DOUBLE-PISTON SEMI-ROTARY ACTUATOR (FESTO DRRD-25-180-FH-PA WITH GEAR RACKS AND A PINION[1]) AND DEFINITION OF DESIGN PARAMETERS.

TABLE 1: MAIN ACTUATOR PROPERTIES.

Property	Symbol	Value
Maximum angular deflection	$\beta_{\max}$	$\pm 100°$
Maximum operating pressure	$p_{\max}$	8 bar
Theoretical actuator moment at 6 bar	M_{nominal}	5.1 N m
Main actuator dimensions ($L \times W \times H$)	L	132 mm
	W	73.2 mm
	H	44.7 mm

The selected actuator is a double-piston semi-rotary actuator with two gear racks and a pinion (DRRD-25-180-FH-PA from Festo). Figure 2 shows a cross-sectional view of the actuator, whereas Table 1 lists the main actuator properties. The two pistons are connected to a pinion via gear racks. Due to its double-acting mode of operation, the applied pressure acts simultaneously on both pistons, regardless of the actuator's direction of rotation. The maximum angular deflection of the actuator is $\beta = \pm 100°$ relative to a neutral state, where both pistons are in a central position and the volume in both chambers is equal ($V_1 = V_2$).

The actuator moment

$$M(p_1, p_2) = c_M \Delta p = c_M\,(p_2 - p_1) \tag{1}$$

depends only on a geometrical factor c_M and the pressure difference $\Delta p = (p_2 - p_1)$ between both actuator chambers.

The geometric factor can be approximated by $c_M \approx 2 r_p A$, where r_p is the effective radius of the pinion and A is the cross-sectional area of the pneumatic cylinders, neglecting additional effects such as friction. With the theoretical actuator moment given in Table 1, the factor calculates to $c_M = M_{\text{nominal}}/6\,\text{bar} = 0.85\,\text{N m/bar} = 0.85\text{E}4\,\text{mm}^3$.

2.2 Test Stand

The pneumatic rotary actuator is characterized on a custom-made test stand. The test stand is designed so that the pressure and volume in both counteracting chambers can be precisely controlled and different external loads can be applied. In addition,

[1]Festo, "Semi-rotary drives DRRD, twin pistons," 2022, https://www.festo.com/media/pim/126/D15000100122126.pdf [retrieved 19 October 2023].

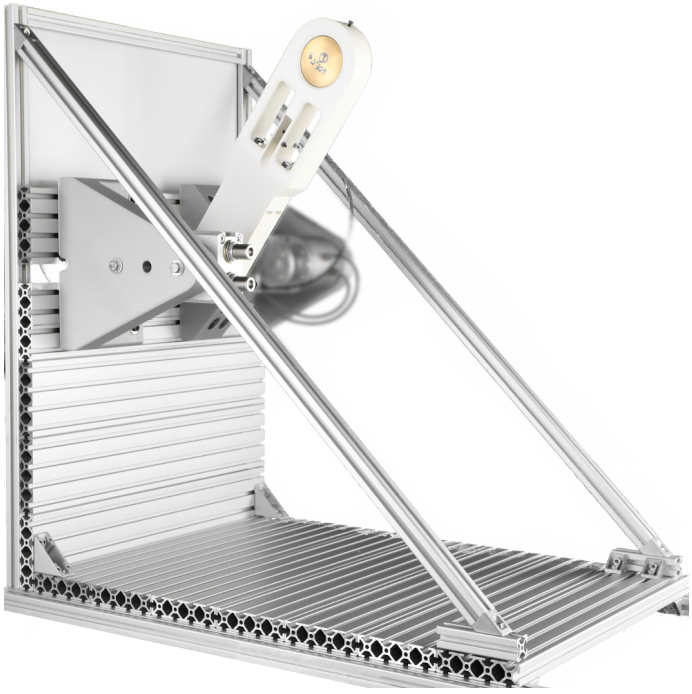

FIGURE 3: PNEUMATIC ROTARY ACTUATOR AND LEVER ARM MOUNTED IN THE TEST STAND.

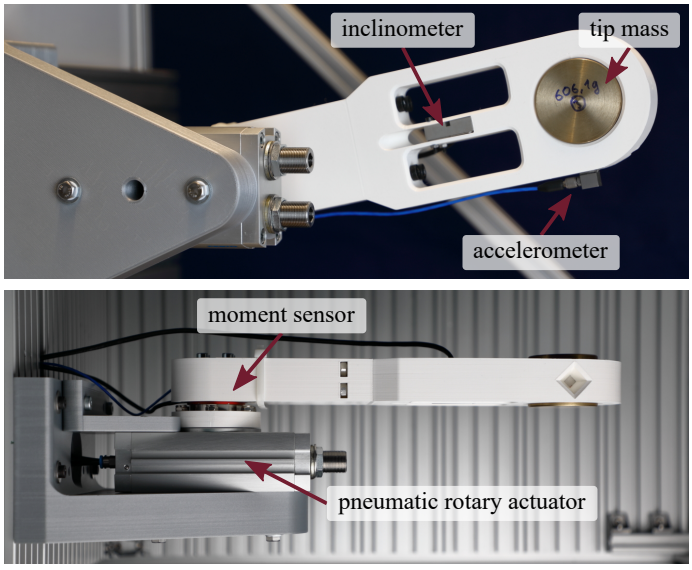

FIGURE 4: DETAIL VIEW OF THE TEST STAND HIGHLIGHTING THE PNEUMATIC ROTARY ACTUATOR, ATTACHED LEVER ARM, INSERTED TIP MASS, AND INSTRUMENTATION.

the pressure in both chambers, the deflection angle, the actuator moment, and the acceleration of the lever arm are measured.

Figure 3 depicts the test stand and shows mechanical components to apply external loads. The rotary actuator is fixed to the frame of the test stand, whereas external loads are applied by adding different masses m_{tip} to the tip of a lever arm ($L_{\text{arm}} = 250\,\text{mm}$, $m_{\text{arm}} = 0.26\,\text{kg}$, $L_{\text{arm,center}} = 128\,\text{mm}$) that is connected to the actuator's flange shaft. Figure 4 is a detail view of the test stand highlighting the mechanical components and

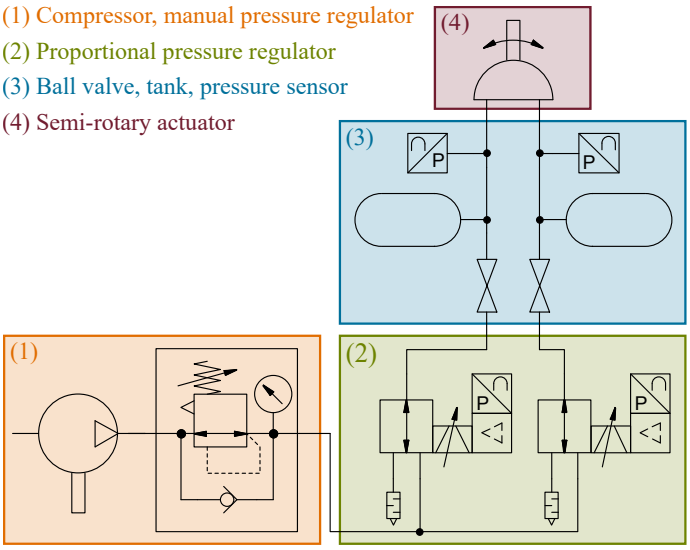

FIGURE 5: PNEUMATIC CIRCUIT OF THE ROTARY ACTUATOR.

sensors. A moment sensor (DC 50-Y2 from KERN & SOHN) is installed at the interface between the lever arm and rotary actuator and an inclinometer (AIT-0101-60 from Althen) measures the arm's deflection angle. An accelerometer (type 4507-B from Brüel & Kjær) is used to measure the dynamic actuator behavior.

Next to the mechanical components, the test stand consists of a pneumatic circuit and an electronic circuit. Figure 5 schematically shows the pneumatic circuit. The compressed air is provided by a compressor and an upstream manual pressure regulator controls the inlet pressure. The pressure in both actuator chambers is controlled by two directly actuated proportional pressure regulators (VPPI-5L-3-G18-0L10H-V1-S1D from Festo). The actuator chambers can be decoupled from the pressure regulators by closing manual ball valves. The tanks represent the variable volumes in the cylinders of the rotary actuators plus the volumes of the tubes from the actuator chambers up to the ball valves. Two pressure sensors (SPAN-P10R-Q4-PNLK-PNVBA-L1 from Festo) are connected in proximity to the chambers of the rotary actuator.

In addition to the pneumatic circuit, there is an electronic circuit for controlling the proportional pressure regulators and processing sensor data. The electronic circuit uses a microcontroller (Arduino Mega 2560) to establish communication between the test stand and a Python-based control environment.

2.3 Test Matrix and Operating Modes

The quasi-static examination of the pneumatic rotary actuator is carried out using two different operating modes, i.e. with two different pneumatic setups. The first mode with open ball valves serves to prove the actuator's zero-stiffness properties, whereas the second mode with closed ball valves allows targeted adjustment of the actuator stiffness. In addition, preliminary dynamic investigations are conducted.

2.3.1 Pressure-Regulated Mode. The first operating mode is pressure-regulated with all valves open to obtain the actuator's complete operating envelope. In this mode, the system can be represented by an isobaric process because the pressure remains constant during actuator deflection since the open valves allow air to enter and exit the actuator chambers. The experiment is a full factorial design covering the entire design space of input pressures p_1 and p_2 and external masses m_{tip} while sensing actuator moment M and angular deflection β. One research hypothesis is that a pneumatic actuator exhibits zero stiffness in a pressure-regulated mode because the moment depends only on the pressure difference between the two actuator chambers, as indicated by Eq. (1), and the actuator moves into one of its end stops when the external moment exceeds the actuator moment. This experiment also serves the validation of the test stand and the calibration of all sensors and electronic components.

2.3.2 Adaptive-Stiffness Mode. In the second operating mode, the ball valves are closed after setting an initial pressure state. The initial pressure state (p_{1n} and p_{2n}) is selected in order to achieve a neutral actuator position ($\beta = 0°$) for a specific external load. After closing the valves, the external load is varied by changing the applied mass m_{tip} at the tip of the lever arm, and the deflection and moment responses are measured. The second operating mode aims to evaluate the hypothesis that the stiffness of pneumatic rotary actuators can be adjusted by controlling the mass flow into the actuator chambers, as proposed by Zheng et al. [17] for pneumatic linear actuators.

With closed valves, the system can be approximated by an adiabatic process because a rotation of the actuator shifts the pistons, changing the volume of the two actuator chambers. For an adiabatic process, the ideal gas equation $pV = mRT$ results in

$$p_1 V_1^{\gamma} = p_{1n} V_n^{\gamma} = \text{constant}, \tag{2}$$

where γ is the heat capacity ratio of the working fluid. For the calculations to be carried out in pneumatics, the mean heat capacity ratio of air is $\gamma = 1.4$ with sufficient accuracy [18].

Deflection induces a volume change and the volume change therefore causes a pressure change that is measured with the two pressure sensors. The volumes

$$V_1(\beta) = V_n - \Delta V \beta \tag{3}$$

and

$$V_2(\beta) = V_n + \Delta V \beta \tag{4}$$

of both actuator chambers only depend on the actuator position, i.e the angular deflection β. Herein, the volume $V_n = 20.5\,\text{cm}^3$ is the volume in the actuator's neutral $\beta = 0°$ position including the tube volume from the actuator chambers up to the ball valves and $\Delta V = 13\,\text{cm}^3/90°$ is the volume change due to actuator rotation.

With the Eqs. (2) to (4), the actuator moment

$$\begin{aligned} M(\beta) &= c_M \left(p_{2n} \left(\frac{V_n}{V_2(\beta)} \right)^{\gamma} - p_{1n} \left(\frac{V_n}{V_1(\beta)} \right)^{\gamma} \right) \\ &= c_M \left(p_{2n} \left(\frac{V_n}{V_n + \Delta V \beta} \right)^{\gamma} - p_{1n} \left(\frac{V_n}{V_n - \Delta V \beta} \right)^{\gamma} \right) \end{aligned} \tag{5}$$

can be expressed as a function of the angular deflection β rather than the pressure difference $\Delta p = (p_2 - p_1)$ as in Eq. (1).

Knowing the initial pressure state (p_{1n} and p_{2n}), the actuator moment can be analytically predicted without measuring the

pressure change in the actuator chambers. Equation (5) directly calculates the actuator's working graph describing the actuator's load-bearing and deformation capacity.

In analogy to a torsion spring, the actuator's rotational stiffness K is the ratio of external moment, i.e. negative actuator moment M, to angular deflection β. The partial derivative

$$K(\beta) = \frac{-\partial M(\beta)}{\partial \beta} = c_M \Delta V \left(\frac{p_{2n} V_n^\gamma}{(V_n + \Delta V \beta)^{\gamma+1}} + \frac{p_{1n} V_n^\gamma}{(V_n - \Delta V \beta)^{\gamma+1}} \right) \quad (6)$$

of Eq. (5) leads to an analytical expression for the actuator stiffness, which allows to deduce the governing parameters affecting K.

2.3.3 Actuator Dynamics. Further preliminary investigations are aimed at characterizing the dynamic actuator behavior. The natural frequencies and the damping ratio can be determined by measuring the acceleration tangentially to the rotation of the lever arm after manually deflecting the actuator into its $\beta = -90°$ position to initiate free vibration.

The damped natural frequency $f_d = 1/T_d$ is the reciprocal of the period T_d of the oscillation, whereas the undamped natural frequency $f_0 = f_d/\sqrt{1-\xi^2}$ is slightly larger than f_d. Here, ξ is the damping ratio that can be be determined from the logarithmic decrement of the decay behavior [19].

Alternatively, the natural frequency of a torsional oscillator can be estimated from the quasi-static tests if the rotary actuator stiffness K and the oscillating masses are known. In this case, the natural frequency is calculated to

$$f_0 = \frac{1}{2\pi} \sqrt{\frac{K}{J}}, \quad (7)$$

where J is the moment of inertia. By approximating the lever arm as a simple pendulum, the moment of inertia $J = m_{\text{tip}} L_{\text{arm}}^2 + m_{\text{arm}} L_{\text{arm,center}}^2$ can be superposed by the tip mass and the length, mass, and center length of the lever arm.

3. RESULTS

This section shows the test results and comparison with analytical prediction functions for actuator moment and stiffness and the wingtip's natural frequencies. The results originate from operation in two quasi-static modes and from initial dynamic tests.

3.1 Pressure-Regulated Mode

When the pneumatic actuator is operated in pressure-regulated mode, constant pressure is applied in the actuator chambers. The operating envelope is evaluated with a control scheme by setting a constant tip mass m_{tip} and a constant pressure p_1 in the downward-acting actuator chamber, while gradually increasing the pressure p_2 in the upward-acting actuator chamber. At the beginning of the control loop, the actuator is at its end stop at $\beta \approx -90°$ due to the gravity force of m_{tip} and the moment generated by the pressure p_1. Applying a counteracting moment by increasing the pressure p_2 causes upward deflection into an equilibrium position, where the actuator moment $M(p_1, p_2)$ equals the moment $M_{\text{external}} \approx m_{\text{tip}} g L_{\text{arm}} \cos\beta$ generated by the external mass. This inner control loop is stopped when β exceeds 20°

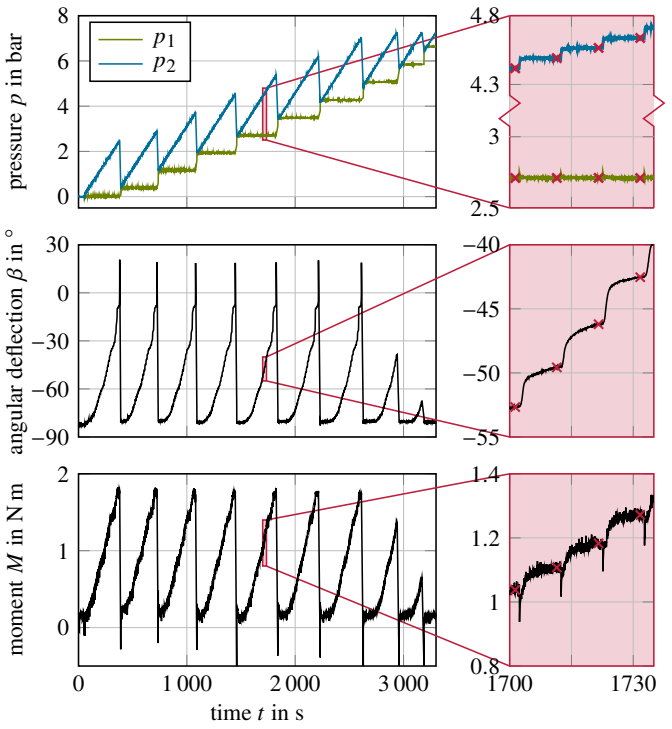

FIGURE 6: THE MEASURED DATA ARE THE PRESSURES p_1 AND p_2, THE ANGULAR DEFLECTION β AND THE MOMENT M OVER THE TIME t. THE CURVES SHOW THE DATA FOR A TIP MASS OF $m_{\text{tip}} = 0.6$ kg. THE MARKERS IN THE DETAILED VIEWS INDICATE THE MEAN VALUES OVER THE LAST 2 s OF EACH MEASUREMENT POINT. ALL PRESSURE VALUES ARE PRESENTED RELATIVE TO AMBIENT PRESSURE.

because further increasing the angle and thus reducing the effective lever arm will cause actuator movement into its end stop at $\beta \approx 90°$. After depressurizing p_2 and successively increasing the pressure p_1, a new control loop is started increasing p_2 again.

Figure 6 shows the data as measured by the pressure sensors, inclinometer, and moment sensor for a tip mass of $m_{\text{tip}} = 0.6$ kg. Each measurement point (each combination of p_1 and p_2) is held for 10 s and mean values are calculated over the last 2 s of each 10 s interval to only use information during static equilibrium. The angular deflections are limited to $\beta = \pm 75°$ due to the range to which the inclinometer is calibrated. The figure also shows that at very large pressures p_1, the zero deflection $\beta = 0°$ is not reached because the actuator moment induced by $\Delta p = p_2 - p_1$ is smaller than the moment generated by the external mass.

The angular deflection β and moment M can be represented as a function of the actuator pressures p_1 and p_2 by plotting the mean values of each measurement point, as shown in Fig. 7. The angular deflection β of a given pressure state increases with decreasing tip mass m_{tip} (Fig. 7a), whereas the actuator moment M is only a function of the actuator pressures independently of the external load (Fig. 7b). The response surfaces of $\beta(p_1, p_2)$ for each m_{tip} can be well approximated by cubic polynomials ($R^2 \geq 0.98$ for each fit). In contrast, the moment is accurately approximated

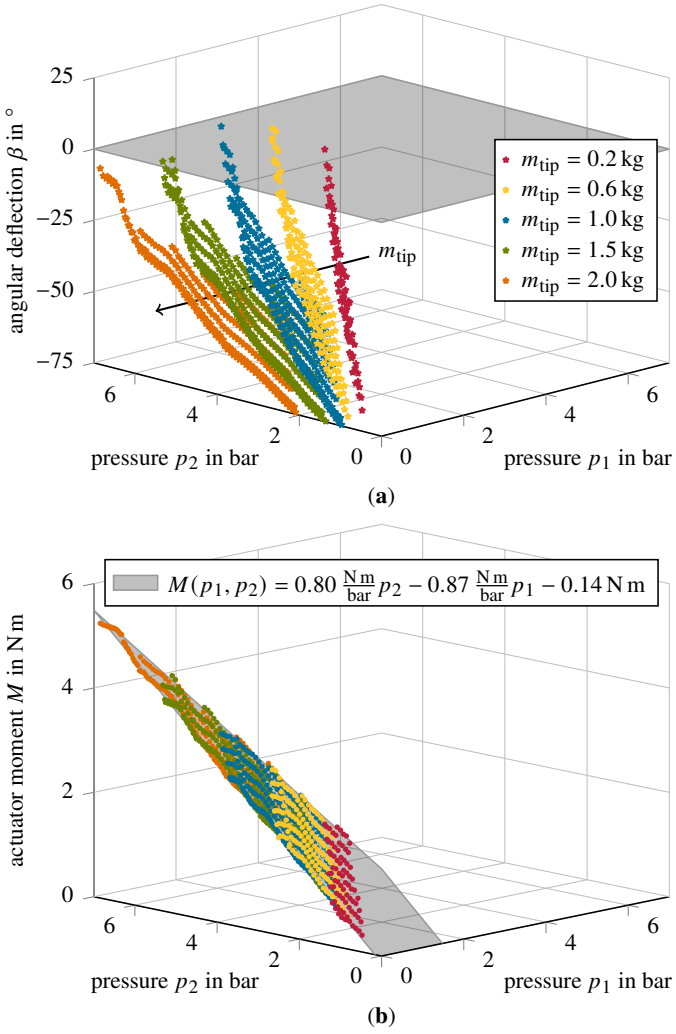

FIGURE 7: MEAN VALUES OF EACH MEASUREMENT POINT REPRESENTING THE ANGULAR DEFLECTION β AND MOMENT M AS A FUNCTION OF THE ACTUATOR PRESSURES p_1 AND p_2.

by the linear prediction function

$$M(p_1, p_2) = 0.80 \frac{\text{N m}}{\text{bar}} p_2 - 0.87 \frac{\text{N m}}{\text{bar}} p_1 - 0.14\,\text{N m} \quad (8)$$

combing all data points regardless of m_{tip} ($R^2 = 0.998$). This function agrees well with Eq. (1) but the constant factors in Eq. (8) are slightly offset from the theoretical value $c_M = 0.85\,\text{N m/bar}$, possibly due to friction because friction generates a force that counteracts the actuator movement.

Figure 8 shows the actuator's working graph, i.e. the actuator moment M as a function of the angular deflection β. The data points in the figure are interpolated from the measured mean values of M and β for selected pressure states, whereas the dashed lines are calculated using the prediction function given in Eq. (8). The data points from the experimental curves agree well with the predicted constant moments. Since the actuator stiffnesses are given by the slopes of the moment–deflection curves, the figure supports the hypothesis that a pressure-regulated pneumatic rotary actuator exhibits zero stiffness regardless of its pressurization and external loading.

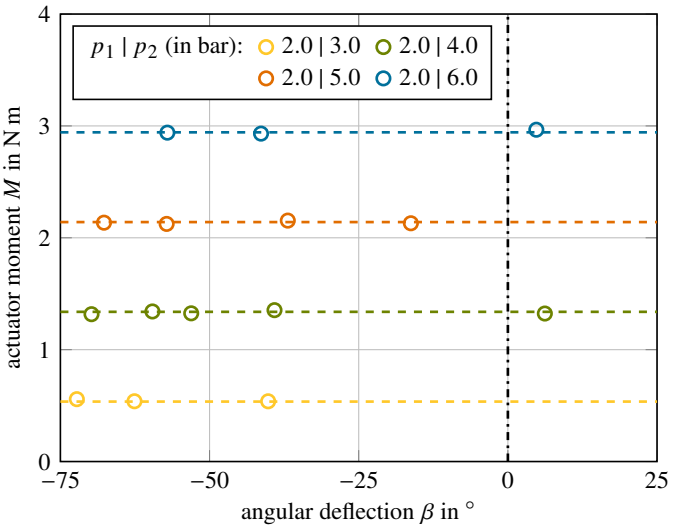

FIGURE 8: WORKING GRAPH FROM THE PRESSURE-REGULATED MODE WITH ALL VALVES OPEN. IN THIS MODE, THE ACTUATOR EXHIBITS ZERO STIFFNESS INDEPENDENT OF ITS PRESSURIZATION OR LOADING. THE DASHED LINES ARE PREDICTIONS CALCULATED WITH EQ. (8) FOR THE SELECTED PRESSURE STATES.

3.2 Adaptive-Stiffness Mode

Whereas the actuator stiffness has been proven to always be zero in the pressure-regulated operating mode, adaptive non-zero actuator stiffness can be realized by controlling the effective volumes of the actuator chambers. In this mode, the ball valves that limit the mass flow into the actuator chambers are closed after setting an initial pressure state, and then the tip mass m_{tip} is varied. Closing the valves maintains a constant air mass in the system so that the volume change due to actuator deflection causes a pressure change.

Figure 9 shows the actuator's working graph obtained for three different pressure states. All pressure states are selected to provide zero actuator deflection together with an applied tip mass of $m_{tip} = 0.6\,\text{kg}$. Therefore, all curves intersect at $\beta = 0°$. The curves are shown for both the system with open or closed ball valves after initial pressurization. The system with open valves represents an isobaric process approximated by Eq. (1), whereas the system with closed ball valves assumes adiabatic behavior approximated by Eq. (5).

The moment–deflection curves of the system with open ball valves in Fig. 9 exhibit zero-stiffness similar to the curves in Fig. 8, whereas the system with closed ball valves features non-zero stiffness. The stiffness K at $\beta = 0°$ indicated in the figure is calculated with Eq. (6) and increases with increasing actuator pressures. In contrast, the moment $M(\beta = 0°)$ at zero deflection is independent of the pressure state. The experimental results agree very well with the analytical prediction functions that require only the initial pressure states and geometric actuator specifications as input parameters.

Next to the simultaneous variation of the pressures in both actuator chambers presented in Fig. 9, Fig. 10 shows the actuator's moment–deflection curves for variable pressure differences between both actuator chambers. Here, the initial pressure states

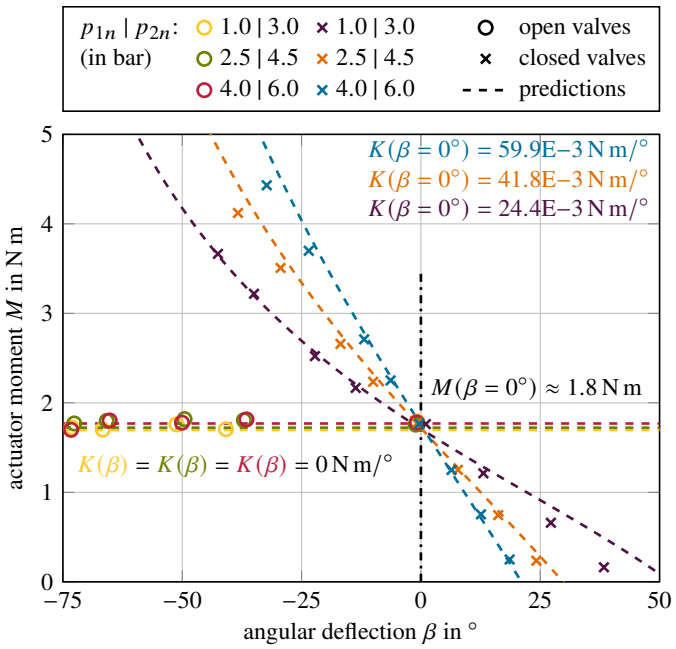

FIGURE 9: WORKING GRAPH FROM THE ADAPTIVE-STIFFNESS MODE WITH ALL VALVES OPEN (ISOBARIC PROCESS) OR CLOSED (ADIABATIC PROCESS). A TIP MASS OF $m_{\text{tip}} = 0.6\,\text{kg}$ IS APPLIED IN THE ZERO-DEFLECTION STATE FOR INITIAL PRESSURIZATION. THE DASHED LINES ARE PREDICTIONS CALCULATED WITH EQ. (1) OR EQ. (5), RESPECTIVELY.

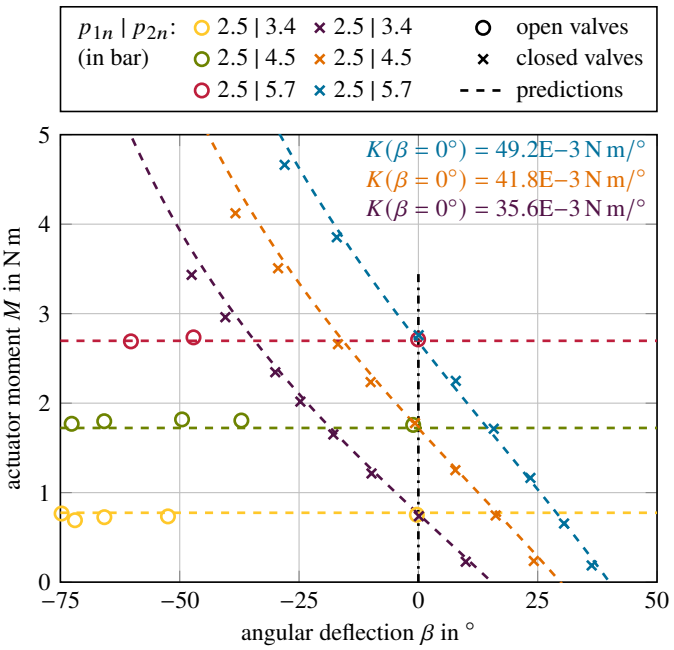

FIGURE 10: WORKING GRAPH FROM THE ADAPTIVE-STIFFNESS MODE FOR DIFFERENT PRESSURE DIFFERENCES BETWEEN BOTH ACTUATOR CHAMBERS. THE ZERO-DEFLECTION STATES FOR INITIAL PRESSURIZATION CORRESPOND TO TIP MASSES OF $m_{\text{tip}} = 0.2\,\text{kg}$, $0.6\,\text{kg}$ AND $1.0\,\text{kg}$. THE DASHED LINES ARE PREDICTIONS CALCULATED WITH EQ. (1) OR EQ. (5), RESPECTIVELY.

are selected to achieve a zero-deflection position for different tip masses ($m_{\text{tip}} = 0.2\,\text{kg}$, $0.6\,\text{kg}$ and $1.0\,\text{kg}$) and therefore different pressure differences. The figure shows that increasing the pressure p_{2n} at constant p_{1n} increases both actuator moment and stiffness.

The comparison of the measured and predicted actuator characteristics in Fig. 9 and Fig. 10 confirms that the actuator behavior of the pneumatic system with closed ball valves can be well predicted by an adiabatic process. Therefore, the analytical equations derived for the adiabatic process are well suited to deduce the governing parameters that affect the actuator characteristics. The evaluation of Eq. (5) and Eq. (6) at $\beta = 0°$ results in

$$M(\beta = 0°) = c_M\,(p_{2n} - p_{1n}) \tag{9}$$

and

$$\begin{aligned} K(\beta = 0°) &= c_M \Delta V \left(\frac{p_{2n} V_n^{\gamma}}{(V_n)^{\gamma+1}} + \frac{p_{1n} V_n^{\gamma}}{(V_n)^{\gamma+1}} \right) \\ &= \frac{c_M \Delta V}{V_n}\,(p_{2n} + p_{1n}) \end{aligned} \tag{10}$$

for the actuator moment and stiffness. The equation of the actuator moment of the adiabatic process equals Eq. (1) of the isobaric process at $\beta = 0°$.

Actuator moment increases with increasing pressure difference $\Delta p = (p_2 - p_1)$, while actuator stiffness increases by either increasing p_{1n} or p_{2n}. In addition, actuator stiffness increases with increasing ratio of $\Delta V / V_n$, i.e. decreasing volume of the actuator chambers. Moreover, actuator moment and stiffness both increase with increasing geometric factor c_M. It should be noted, however, that c_M is a factor specific to the actuator geometry, which also indirectly influences the actuator volume.

3.3 Actuator Dynamics

The natural frequencies and damping ratios of the wingtip hinge assembly are determined from the acceleration measured during free vibration for different test configurations. Figure 11 exemplarily shows the actuator oscillation for a tip mass of $m_{\text{tip}} = 0.6\,\text{kg}$ and actuator pressures of $p_{1n} = 1.0\,\text{bar}$ and $p_{2n} = 3.0\,\text{bar}$. The damping ratio is determined from the exponent of the exponential fit through the peaks of the curve. The peak at $t = 0\,\text{s}$ is ignored due to slight differences in initial conditions between all experiments. The figure shows that the absolute values of the normalized acceleration are used to increase the number of peaks for the exponential fit.

The dynamic tests are performed for all configurations shown in Fig. 9 and Fig. 10. In addition, the natural frequencies f_0 are calculated with Eq. (7) using the stiffnesses $K(\beta = 0°)$ from the quasi-static tests. Table 2 summarizes the results of the quasi-static and dynamic tests. The natural frequencies increase with increasing actuator stiffness or decreasing tip mass, whereas the damping ratio decreases with increasing stiffness or mass.

The natural frequencies from the quasi-static and dynamic tests deviate from each other by around 20% to 30%. One reason for the underestimation in the quasi-static tests is that the actuator stiffness was assumed constant in the calculation. However, Fig. 9 and Fig. 10 show that the stiffness is not constant but a nonlinear function of the angular deflection and increases with increasing

TABLE 2: NATURAL FREQUENCIES AND DAMPING RATIO OF THE WINGTIP HINGE WITH PNEUMATIC ROTARY ACTUATOR.

Test configuration			From quasi-static test		From dynamic test		
Pressure p_{1n}	Pressure p_{2n}	Mass m_{tip}	Stiffness $K(\beta = 0°)$	Undamped natural frequency [a] f_0	Damped natural frequency f_d	Damping ratio ξ	Undamped natural frequency f_0
1.0 bar	3.0 bar	0.6 kg	24.4E−3 N m/°	0.92 Hz	1.31 Hz	0.144	1.32 Hz
2.5 bar	4.5 bar	0.6 kg	41.8E−3 N m/°	1.20 Hz	1.59 Hz	0.123	1.60 Hz
4.0 bar	6.0 bar	0.6 kg	59.9E−3 N m/°	1.44 Hz	1.81 Hz	0.121	1.83 Hz
2.5 bar	3.4 bar	0.2 kg	35.6E−3 N m/°	1.75 Hz	2.20 Hz	0.141	2.22 Hz
2.5 bar	4.5 bar	0.6 kg	41.8E−3 N m/°	1.20 Hz	1.59 Hz	0.123	1.60 Hz
2.5 bar	5.7 bar	1.0 kg	49.2E−3 N m/°	1.03 Hz	1.36 Hz	0.125	1.37 Hz

[a] calculated with Eq. (7)

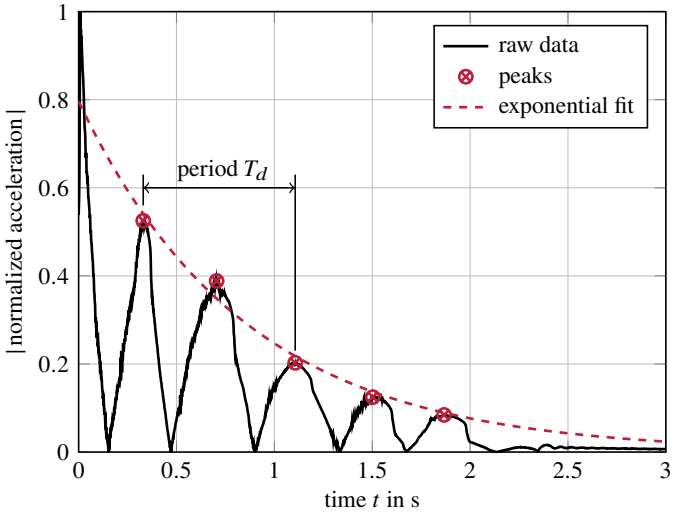

FIGURE 11: ABSOLUTE VALUES OF THE ACCELERATION MEASURED DURING FREE VIBRATION FOR A TIP MASS OF m_{tip} = 0.6 kg AND ACTUATOR PRESSURES OF p_{1n} = 1.0 bar AND p_{2n} = 3.0 bar.

positive or negative deflections. With increasing stiffness, the natural frequencies increase according to Eq. (7) and the deviations relative to the dynamic tests decrease. Further explanations for the deviation are due to neglecting effects such as friction.

Overall, the models agree well when considering the simplifications used. Therefore, calculating the natural frequency from the stiffness of the adiabatic process is a good starting point for a preliminary design of a pneumatic rotary actuator for application in folding wingtip devices.

4. IMPLICATIONS FOR FOLDING WINGTIP DEVICES

Having shown the inherent properties of a rotary actuator on a small scale, these findings have yet to be scaled to loads occurring during aircraft operation. This section therefore draws implications for implementing pneumatic rotary actuators as multifunctional wingtip actuators on highly efficient HAR aircraft.

The bending moment acting on the wingtip device depends on various factors such as the aircraft mass, wingspan, and hinge line position. In current research activities on in-flight folding wingtips, free-flapping wingtips are being validated on aircraft the size of typical business jets, such as by Airbus [10] on the *eXtra Performance Wing* demonstrator. Therefore, in a previous study [15], the authors investigated the performance of actuated adaptive wingtips on a Cessna Citation X with 19.4 m wingspan using aeroelastic analysis. The aeroelastic analysis yielded a wingtip bending moment of $M_{wt} \approx 800\,\text{N m}$ at the wingtip hinge line at 90% span in a static 1.0 g cruise load case. The hinge-line position of 90% span was selected as a reasonable trade-off between loads and performance, as recommended in [20].

Sufficient actuator moment is required to maintain the aerodynamically efficient cruise shape of the wing, whereas actuator stiffness defines the equilibrium position of the deflected wingtip at elevated loads. The pneumatic rotary actuator must therefore counter the wingtip bending moment of $M_{wt} \approx 800\,\text{N m}$ in cruise flight. When the wing load increases during flight maneuvers or gust encounters, the wingtip folds upward, which prevents an increase in wingtip lift and bending moment [15]. The moment of the investigated pneumatic rotary actuator (DRRD-25-180-FH-PA from Festo) at maximum pressurization is with $M(p_1 = 0\,\text{bar}, p_2 = 8\,\text{bar}) = 6.8\,\text{N m}$ far below the required moment. However, the investigated actuator is only a functional demonstrator and is not intended to represent a realistic design of a wingtip hinge.

For the use of pneumatic rotary actuators as multifunctional wingtip devices, the actuator's load-bearing capacity must be designed in accordance with real flight loads. The allowable actuator moment can be increased in various ways: by connecting several actuators in parallel, optimizing the actuator geometry, or increasing the maximum operating pressure. Equation (9) shows that the moment of each rotary actuator in the zero-deflection cruise position is only a function of the pressure difference between both actuator chambers and a geometric factor c_M. The factor c_M describes how much moment the actuator can generate at a certain input pressure and depends only on the geometric design of the actuator. To put these principles into a practical context, consider the example of a larger model of the same actuator type like the DRRD-63-180-FH-Y9A from Festo, which can attain an actuator moment as high as 187 N m at a maximum input pressure of 10 bar. However, this increase in moment capacity comes with the downside of added mass and size. A more compact and lightweight solution is possible with a custom-made actuator design optimized for the specific application. Gener-

ally, pneumatic and hydraulic actuators are distinguished by a high power density compared to other actuator types [21], which proves their viability for the presented application. In addition, the structural mass added by the wingtip device is not expected to be critical in aircraft design, since its outboard position combined with its load alleviation capability reduces WRMB and therefore wing mass. The use of several actuators in parallel offers the additional advantage of increasing the wingtip's torsional stiffness.

An alternative approach to greatly increase actuator moment is to switch from a pneumatic to a hydraulic system. Hydraulic systems allow significantly higher operating pressures, which are above 200 bar in already existing, typical aircraft systems [22]. However, operating a hydraulic system in the adaptive-stiffness mode requires additional effort. In a hydraulic system, the compressible volume is decoupled from the actuator size, as the hydraulic fluid itself is incompressible. Therefore, a gas-filled expansion tank must be integrated into the hydraulic system in order to enable the volume-dependent pressure change. Alternatively, adaptive stiffness of a hydraulic actuator could be achieved with a closed-loop control that actively controls the actuator pressures as a function of the actuator's angular deflection.

Actuator stiffness determines the extent of deflection under an acting load and governs the dynamic actuator characteristics. A free-flapping wingtip with zero hinge stiffness moves into an equilibrium position in which the wingtip generates zero lift causing significant load alleviation [15]. In contrast, targeted adjustment of actuator stiffness allows the use of passive load alleviation during take-off and landing without fearing an abrupt loss of lift and to adapt the passive load alleviation to the environmental conditions. The controlled introduction of actuator stiffness prevents the actuator from deflecting into its end stop. This is particularly beneficial under severe off-design loads, such as sideslip or lateral gusts, which would require special consideration with free-flapping wingtips as these may become unstable [23, 24].

Different operating scenarios have different requirements on the wingtip hinge stiffness. In passive scenarios, on the one hand, the stiffness must be high enough to maintain the optimal wing shape during cruise conditions, even in the face of minor turbulence or small gusts. High stiffness prevents the wingtip from freely oscillating and potentially coupling with other vibration modes of the aircraft causing flutter [9]. On the other hand, the stiffness must be low enough, ideally zero, to allow for load alleviation during more significant disturbances. In active scenarios, for enhanced load alleviation, the actuator can provide support by amplifying the passive movement beyond the equilibrium position of the free-flapping wingtip, further improving load alleviation. This is effectively equivalent to a negative stiffness that augments the wingtip's natural movement.

This study showed that targeted adjustment of the stiffness of pneumatic rotary actuators is possible by shutting off the mass flow into the actuator chambers, whereas in a pressure-regulated operation mode, the actuator stiffness is always zero. However, actuator stiffness could also be induced by implementing a control scheme that actively controls the actuator pressures as a function of the angular deflection β. With such a closed-loop control system, actuator moment and stiffness can be varied arbitrarily and independently within the actuator's operating envelope without the need to change the pneumatic setup, e.g. by closing valves to limit airflow into the actuator chambers. Such an active mode of operation is the basis for using pneumatic wingtip actuators as flight control surfaces because it allows a controlled adjustment of the wingtips' cant angles. Besides the passive load alleviation mode, actively adjusting actuator moment and stiffness to the flight mission and weather conditions transforms folding wingtips into multifunctional actuated adaptive wingtips. This clears the path for the incorporation of additional functionalities into the wingtip hinge such as advanced flight control, mission adaptability, enhanced load alleviation, or flutter suppression.

5. CONCLUSION

This study demonstrated the significant stiffness adaptivity of pneumatic rotary actuators in experiments and derived simple analytical equations for identifying governing factors influencing the stiffness and moment of the actuator as well as the wingtip's natural frequencies. The characteristics of pneumatic rotary actuators can be accurately described by an isobaric or adiabatic process, depending on the pneumatic setup. With these equations, implications for the design and operation of multifunctional wingtip actuators were drawn. The next steps in the realization of multifunctional actuated adaptive wingtips are the extension of the dynamic investigations with regards to gusts and flutter and building an up-scaled version of the actuator that achieves the load-bearing capacity required for implementation on an aircraft like a Cessna Citation.

ACKNOWLEDGMENTS

This research was funded by the German Federal Ministry for Economic Affairs and Climate Action (BMWK) under project number 20A2103D (MuStHaF) and by the Deutsche Forschungsgemeinschaft (DFG, German Research Foundation) – Project-ID 498601949 – TRR 364.

REFERENCES

[1] Afonso, F., Vale, J., Oliveira, E., Lau, F. and Suleman, A. "A review on non-linear aeroelasticity of high aspect-ratio wings." *Progress in Aerospace Sciences* Vol. 89 (2017): pp. 40–57. DOI 10.1016/j.paerosci.2016.12.004.

[2] International Civil Aviation Organization. "Annex 14 - Aerodromes - Volume I: Aerodromes Design and Operations." (2022).

[3] Federal Aviation Administration. "Advisory Circular - Airport Design (AC 150/5300-13B)." (2022).

[4] American Society of Mechanical Engineers. "Wing Folding Mechanism of the Grumman Wildcat: An American Society of Mechanical Engineers Historic Mechanical Engineering Landmark." (2006). Accessed 24 October 2023, URL https://www.asme.org/about-asme/engineering-history/landmarks/238-grumman-wildcat-sto-wing-wing-folding.

[5] Ajaj, R. M. "Flight Dynamics of Transport Aircraft Equipped with Flared-Hinge Folding Wingtips." *Journal of Aircraft* Vol. 58 No. 1 (2021): pp. 98–110. DOI 10.2514/1.C035940.

[6] Meyer, P., Traub, H. and Hühne, C. "Actuated adaptive wingtips on transport aircraft: Requirements and preliminary design using pressure-actuated cellular structures." *Aerospace Science and Technology* Vol. 128 (2022): 107735. DOI 10.1016/j.ast.2022.107735.

[7] Wilson, T., Kirk, J., Hobday, J. and Castrichini, A. "Small scale flying demonstration of semi aeroelastic hinged wing tips." *International Forum on Aeroelasticity and Structural Dynamics (IFASD 2019)*: pp. 1115–1133. Savannah, Georgia, 9-13 June, 2019.

[8] Wilson, T., Kirk, J., Hobday, J. and Castrichini, A. "Update on AlbatrossONE Semi Aeroelastic Hinge Small Scale Flying Demonstrator Project." *International Forum on Aeroelasticity and Structural Dynamics (IFASD 2022)*: pp. 47–68. Madrid, Spain, 13-17 June, 2022.

[9] Castrichini, A., Siddaramaiah, V. H., Calderon, D. E., Cooper, J. E., Wilson, T. and Lemmens, Y. "Preliminary investigation of use of flexible folding wing tips for static and dynamic load alleviation." *The Aeronautical Journal* Vol. 121 No. 1235 (2017): pp. 73–94. DOI 10.1017/aer.2016.108.

[10] Airbus. "eXtra Performance Wing demonstrator takes off." (2023). Accessed 10 November 2023, URL https://www.airbus.com/en/newsroom/stories/2023-11-extra-performance-wing-demonstrator-takes-off.

[11] Dussart, G. X., Lone, M., O'Rourke, C. and Wilson, T. "In-flight Wingtip Folding: Inspiration from the XB-70 Valkyrie." *International Journal of Aviation, Aeronautics, and Aerospace* Vol. 6 No. 3 (2019): 7. DOI 10.15394/ijaaa.2019.1343.

[12] Benafan, O., Moholt, M. R., Bass, M., Mabe, J. H., Nicholson, D. E. and Calkins, F. T. "Recent Advancements in Rotary Shape Memory Alloy Actuators for Aeronautics." *Shape Memory and Superelasticity* Vol. 5 No. 4 (2019): pp. 415–428. DOI 10.1007/s40830-019-00260-3.

[13] Mills, J. and Ajaj, R. M. "Flight Dynamics and Control Using Folding Wingtips: An Experimental Study." *Aerospace* Vol. 4 No. 2 (2017): 19. DOI 10.3390/aerospace4020019.

[14] Carrillo Córcoles, X., Mertens, C., Sciacchitano, A., van Oudheusden, B. W., De Breuker, R. and Sodja, J. "Effect of Wing Stiffness and Folding Wingtip Release Threshold on Gust Loads." *Journal of Aircraft* Vol. 60 No. 6 (2023): pp. 1917–1936. DOI 10.2514/1.C037108.

[15] Meyer, P., Hühne, C., Bramsiepe, K. and Krüger, W. "Aeroelastic Analysis of Actuated Adaptive Wingtips Based on Pressure Actuation." *Journal of Aircraft* Vol. 61 No. 1 (2024). DOI 10.2514/1.C037390.

[16] Meyer, P., Vorhof, M., Koord, J., Sennewald, C., Cherif, C. and Hühne, C. "Anisotropic flexure hinges: Manufacturing and mechanical characterization for application in pressure-actuated morphing structures." *Composites Part B: Engineering* Vol. 266 (2023): 110967. DOI 10.1016/j.compositesb.2023.110967.

[17] Zheng, H., Wu, M. and Shen, X. "Pneumatic Variable Series Elastic Actuator." *Journal of Dynamic Systems, Measurement, and Control* Vol. 138 No. 8 (2016): 081011. DOI 10.1115/1.4033620.

[18] Grollius, H.-W. *Grundlagen der Pneumatik*, 4th ed. Fachbuchverlag Leipzig im Carl Hanser Verlag, München, Germany (2018).

[19] Sinapius, M., Kletz, B. T. and Opitz, S. "Active Vibration Control." Sinapius, M. (ed.). *Adaptronics – Smart Structures and Materials*. Springer Vieweg, Berlin, Germany (2021): pp. 227–329. DOI 10.1007/978-3-662-61399-3_6.

[20] Delavenne, M., Barriety, B., Vetrano, F., Ferrand, V. and Salaun, M. "Parametric Analysis of an Active Winglet Concept for High Aspect Ratio Wing Using CFD/CSM Computations." *AIAA Aviation 2020 Forum*: pp. 1–17. Virtual, Online Conference, 15-19 June, 2020. DOI 10.2514/6.2020-2662.

[21] Huber, J. E., Fleck, N. A. and Ashby, M. F. "The selection of mechanical actuators based on performance indices." *Proceedings of the Royal Society A: Mathematical, Physical and Engineering Sciences* Vol. 453 No. 1965 (1997): pp. 2185–2205. DOI 10.1098/rspa.1997.0117.

[22] Moir, I. and Seabridge, A. G. *Aircraft Systems: Mechanical, electrical, and avionics subsystems integration*, 3rd ed. John Wiley & Sons, Chichester, West Sussex, UK (2008).

[23] Conti, C., Saltari, F., Mastroddi, F., Wilson, T. and Castrichini, A. "Quasi-Steady Aeroelastic Analysis of the Semi-Aeroelastic Hinge Including Geometric Nonlinearities." *Journal of Aircraft* Vol. 58 No. 5 (2021): pp. 1168–1178. DOI 10.2514/1.C036115.

[24] Cheung, R. C. M., Gu, H., Healy, F., Rezgui, D. and Cooper, J. E. "Lateral Gust Behaviour of Aircraft Incorporating Flared Folding Wingtips." *33rd Congress of the International Council of the Aeronautical Sciences*: pp. 4113–4127. Stockholm, Sweden, 4-9 September, 2022.